

# The importance of a non-deterministic design optimization for predicting real-life propeller performances

Kevin Vidal<sup>1</sup>, Leo Poppelier<sup>2</sup>, Benoit Mallol<sup>1</sup>, Charles Hirsch<sup>1</sup>

<sup>1</sup>NUMECA International, Brussels, Belgium

<sup>2</sup>SIP Marine BV, Drunen, Netherlands

## ABSTRACT

The manufacturing of propellers comes with geometrical variability that lies within predefined tolerances decreed by standardized accuracy classes. Although controlled by these tolerances classes, the variation in the design might result in a degradation of the expected propeller behaviour.

In a classical deterministic design optimization, engineers improve a digital model, without taking into account these variations. Hence a new type of optimization method is recommended whereby the impact of the manufacturing variability, represented by statistical moments, is minimized.

This paper presents a robust non-deterministic optimization of a ducted marine propeller mounted on an inland vessel. In this test case, the statistical moments of the propeller efficiency are optimized while axial thrust is constrained and cavitation occurrence is considered. The manufacturing uncertainties are derived from the ISO geometrical tolerances S-class. Eventually, a robust optimum is compared with a deterministic optimum in order to underline the benefits of the non-deterministic design methodology.

## Keywords

Uncertainty quantification, probabilistic methods, surrogate-based non-deterministic optimization, manufacturing tolerances, ISO 484-2 2015

## 1 INTRODUCTION

In the recent year, the design time has been drastically reduced thanks to modern computing involving computational fluid dynamics (*CFD*) and embedded and automated frameworks for the simulation-based design optimization (*SBDO*). Nowadays, hydrodynamics *SBDO* of a marine propeller is currently run with a unique set of inputs, such as geometry parameters and operating conditions. This overwhelming deterministic approach produces a single value response that mainly drives all the optimization strategies. But the actual operating conditions are subject to uncertainties coming from manufacturing tolerances, operating conditions and long term life cycle involving the slow degradation of materials because of cavitation or fouling. Aware of these variabilities, modern designers currently use tools that generally do not provide means to assess their impacts.

And consequently they need to impose very strict and costly manufacturing tolerances to make sure the newly optimum design is not influenced.

This paper presents a non-deterministic methodology that allows assessing quantitatively the effect of these variabilities, and is applied on the design optimization of a ducted marine propeller. This newly optimization procedure, called *RDO*, aims at improving the performances, but also guaranteeing a stable behaviour given an inputted variability.

Hence, the *RDO* provides a range of confidence with the simulation results and might help future designers in their design strategy.

In this work, two operating conditions are studied and the manufacturing tolerances come from the *ISO 484-2 2015*.

## 2 PRESENTATION OF THE TEST CASE

### 2.1 Background

The background of the project consists in optimizing a propeller mounted on an inland vessel with a single propeller system and twin-blade rudder appendages.



Figure 1: The inland vessel under different loadings.

Table 1: The main particulars of the inland vessel.

AIS vessel type	Tanker - Haz C
LOA x BE	109.7 m x 11.4 m
Deadweight	2810 tons
Year built	2010
Design draught	2.8 m
Max draught	3.35 m
Design speed	5.4 knots (10km/h)
Max speed	6.2 knots (11.5km/h)

The inland vessel market will grow at over 4.5 per cent from 2017 to 2024 (Insights global market 2018), justifying the recent trend at improving the performances of such vessel for economical and ecological reasons (Sihn et al 2015). As a consequence, the optimization of the propulsion device could be an achievable solution for naval architects.

## 2.2 Presentation of the ducted marine propeller

The propeller studied is a fixed pitch ducted propeller where the main characteristics are defined in table 2.

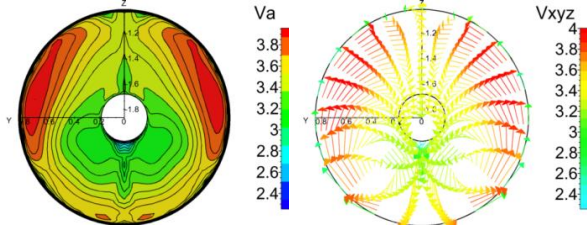


Figure 2: Nominal wake of the ship at design speed.

According to the BAW (2016), all newly designed inland vessels have propellers with a nozzle. The main reason is the capacity to carry on higher thrust loading with better efficiency.

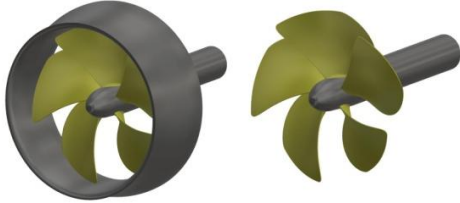


Figure 3: The ducted propeller with and without the nozzle.

The studied case is a replacement propeller for the vessel. No design specifications were formulated for the nozzle, because it is embedded in the hull of the ship (cf. fig.4).



Figure 4: Final propeller mounted on the ship, the duct is part of the hull.

In general practice, this type of propellers is based upon the Wageningen Ka-series ducted propellers. Hence, the empirical formulas, based on  $J$ - $K_t/K_q$ , determine thrust and power as a function of speeds and engine characteristics. The coefficients  $J$ - $K_t/K_q$  are defined as followed:

$$K_t = \frac{T_{propeller} + T_{nozzle}}{\rho n^2 D_{propeller}^4} \quad (1)$$

$$K_q = \frac{Q_{propeller}}{\rho n^2 D_{propeller}^5} \quad (2)$$

$$J = \frac{V_{axial}}{nD} \quad (3)$$

Where  $T$  = axial thrust (N);  $Q$  = torque (Nm);  $\rho$  = water density ( $\text{kg/m}^3$ );  $n$  = revolution rate (rpm);  $D$  = propeller diameter (m); and  $V_a$  = incoming flow velocity (m/s).

The working area of the propeller is eventually defined, and therefore the blade area ratio and the required pitch. Then, the ship resistance is computed in order to extract the wake field (cf. fig.2). This field helps to finalize the design loop by adjusting the section profile, and more shape-determining parameters. Hence the optimization procedure can be applied during those final iterations in the design process.

Table 2: The main particulars of the propeller.

Type	Fixed pitch
Diameter	1.7 m (2.08 m with duct)
Number of blades	5
Mean pitch	2.251 m
Chord length at 0.7R	0.68 m
Revolutions/sec	5.385 rps

## 3 DETERMINISTIC OPTIMIZATION FRAMEWORK

### 3.1 General principle

The most straightforward optimization approach is to sample the design space and use *CFD* at the selected point, and try to find a design for which the performances are better. However, each optimization iteration requires a *CFD* computation, increasing the time and computation power. In this manner, an efficient methodology is implemented in FINE™/Design3D, and relies on two building blocks, pre-exploration of the design space, performed by a design of experiments (*DoE*), and a surrogate assisted optimization.

### 3.2 Design of experiment for design space exploration

The first step consists in pre-exploring the design space, by using a near-random *DoE*. This pre-exploration allows creating a metamodel or a response surface that is going to be used during the optimization. For that purpose a latin hypercube sampling (*LHS*) is applied to sample the design space.

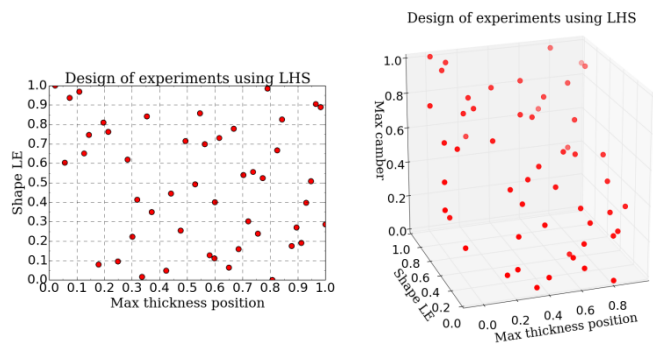


Figure 5: DoE of 30 samples for two and three design parameters.

As the response surface accuracy depends on the *DoE*, the number of initial design to generate is a compromise between:

- a high number of samples creating an accurate approximate model, but refining in area of low interest and requiring more computation power;

- a low number to limit as much as possible the *CFD* effort.

For a full benefit of this pre-exploration, the *DoE* is populated with 5 times the number of design parameters, in this study.

### 3.3 Surrogate model

From the *DoE*, the metamodel can be created. This approximate model, also called surrogate model, provides global design trends. The aim of the surrogate model is to mimic the propeller performances at points in between the *DoE* samples with a significant lower cost than *CFD*.

### 3.4 Deterministic surrogate assisted optimization

The optimizer uses a genetic algorithm (*GA*) to locate the interesting area. *GA* has the advantage to search globally in the design space (Coley 1999), and mimics the natural evolution process by extracting the best design candidates over a population based on the surrogate results. Once the *GA* coupled with the surrogate model finds the expected optimum. A *CFD* simulation is performed in order to check the validity of this expected optimum design and fine-tuned the response surface for higher accurate prediction capacity with the aim of advancing further towards the global optimum. The objectives and constraints formulations can be:

- Single objective, in case of several operating conditions, the objectives and constraints can be aggregated;
- Multi-objectives, where the outcome of the optimization is the Pareto front. The Pareto front represents a set of non-dominated designs, meaning there is no better design for the respective objectives combination.

The non-deterministic optimization, discussed in the next section, shares a common workflow with the deterministic one. The main difference lies on the definition of the objectives and constraints.

## 4 NON DETERMINISTIC OPTIMIZATION FRAMEWORK

Any industrial design is influenced by a superposition of several uncertainties. In order to understand the impact of these uncertainties, an uncertainty quantification (*UQ*) method needs to be applied.

### 4.1 Uncertainty quantification method

#### 4.1.1 Brief technical overview of the methodology

To allow the propagation of uncertainties, the method, used within this work, is the non-intrusive probabilistic collocation method (*NIPCoLM*) (Loeven 2007).

This approach was implemented and successfully applied on the *NASA rotor 37* validation case by Nigro et al (2017).

The basis of this method is formed by the expansion of the solution into Lagrange interpolating polynomials.

The base points are the collocation points, which correspond to the Gauss quadrature points weighted by an input uncertainty defined as probability density function (*PDF*).

In order to compute the Gauss quadrature, the Golub-Welsch algorithm is used to provide the collocation points and it weights (Golub & Welsch 1969).

A system of uncoupled deterministic simulations can be eventually derived.

Once the  $N_p$  uncoupled simulations are solved, statistical moments of any output  $\varphi_i$  are automatically computed by taking the weight  $\omega_i$  from the Gauss quadrature. The mean and variance are calculated as followed:

- For non-centered moments, such as the mean ( $n = 1$ );

$$\mu_{n_{non-centered}} = \sum_{i=1}^{N_p} \omega_i (\varphi_i)^n \quad (4)$$

- For centered moments, such as the variance ( $n = 2$ ).

$$\mu_{n_{centered}} = \sum_{i=1}^{N_p} \omega_i (\varphi_i - \mu_{1_{non-centered}})^n \quad (5)$$

These statistical moments express the measure of the uncertainties influence over the quantities of interest.

#### 4.1.2 Sparse grid quadrature for solving multiple uncertainties

In order to handle multiple uncertainties simultaneously, the *NIPCoLM* is usually applied with a full tensor product. This eventually leads to an exponential number of *CFD* simulations which is referred in the literature by “*the curse of dimensionality*”, and therefore cannot be used at industrial scale.

To solve this issue Nigro et al (2018) applied the sparse grid technique, based on Smolyak’s quadrature method (Smolyak 1963).

The sparse grid technique consists in truncating dimensional function terms higher than a level of accuracy. Thus, Smolyak’s quadrature is not subject to the curse of dimensionality, and therefore offers a more efficient way of approximating function in high dimension, allowing so to make simultaneous treatment of many uncertainties in complex *3D CFD* simulation.

**Table 3: Full tensor product grid with 3 points in each dimension versus Smolyak grids using a level 1.**

Dimension (number of uncertainties)	Tensor product grid (number of <i>CFD</i> )	Smolyak grid Level=1 (number of <i>CFD</i> )
1	3	3
2	9	5
10	59049	21
20	$3^{20}$	41

#### 4.1.3 Sensitivity analysis for understanding the relative uncertainty influence

When facing multiple uncertainties, the analysis of the relative influence of each input uncertainty is an important element. This analysis is based on the scaled sensitivity derivatives, introduced by Turgeon et al (2001), and is used to identify the most important uncertainty over an output quantity.

In practice, the sensitivity derivative is defined as the partial derivative of the solution, from the system of uncoupled equations, with respect to the input uncertain parameter. The result is then scaled by multiplying the standard deviation of the same random input.

The scaled sensitivity derivatives provide so the influence of each parameter separately, so no combined effects are taken into account.

Moreover, by providing a measure of the influence of uncertainties over the output, this analysis allows to reduce the number of uncertain input, by removing input with little influence. This can have the positive effect of using less deterministic simulations.

#### 4.2 Robust design optimization

The main difference between the deterministic and non-deterministic optimization is the definition of the objectives and the constraints. The prior considers single values, and the latter takes into account statistical moments, represented by the mean and the variance (4) and (5). The most direct approach is to apply the *UQ* method for every single design in the *DoE*, hence the surrogate model is constructed based on the statistical moments of each sample. However the cost of the non-deterministic *DoE* corresponds to the cost of the deterministic one times the number of *UQ* simulations. For a usual hundred of samples in the *DoE*, this approach is beyond any industrial application.

For this reason, Nigro et al (2018) proposed the solution to build the *DoE* including both design parameters and uncertainties.

Here is the example of 18 design variables and 4 uncertainties assuming the distribution is symmetric, it gives 9 deterministic simulations to run. Using 3 points in each direction of the *DoE*, we can obtain the following:

- *DoE* with *UQ* simulations:  
 $18 * 3 * 9 = 486$  CFD simulations
- Mixed *DoE*:  
 $(18 + 4) * 3 = 66$  CFD simulations

This gain in the computational time is achieved at the expense of not having the statistical moments directly available in the surrogate model. In this manner, the surrogate is updated with *UQ* simulations during the optimization procedure.

### 5 PRE-OPTIMIZATION STUDY

#### 5.1 Numerical modelling

##### 5.1.1 Grid generation and grid dependency study

AutoGrid5™, used for the meshing, is an automated multi-block structured mesh generator, which gives a high quality mesh on the surface, for a short generation time. In our case a 5 million points mesh is generated in 2 minutes on 4 threads.

Moreover, templates can be used to project same topology grid into newly design geometry shape, which is a main advantage in the frame of an optimization.

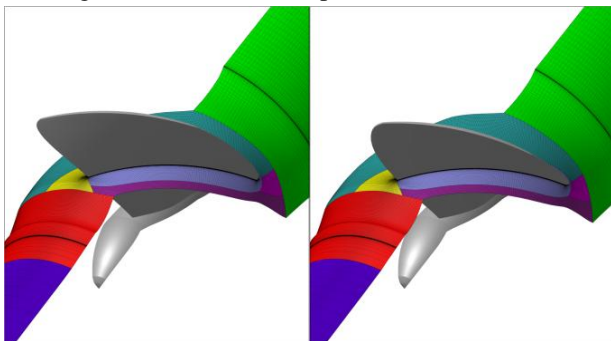


Figure 6: Template in AutoGrid5™ helps to keep the exact same mesh topology for different geometry shape. It can be seen the structured block topology is maintained for 2 different geometries.

A O4H topology is used to generate a series of five nested meshes. The targeted  $Y^+$  is 100, since the study is carried out on full scale. It gives a first layer size normal to the surface equal to  $8e-05$  meters. The O4H grid topology consists in a O-block in the skin block of the blade and H-blocks around the main skin block. The quality of the nested meshes is summarized below (cf. table 4). The meshes are obtained by adjusting the number of points in the O4H topology without modifying the first layer thickness. It shows that the meshing strategy has maintained the high quality mesh and the  $Y^+$  requirements.

Table 4: Overview of the quality of the five nested meshes.

Mesh	1	2	3	4	5
Millions points	3.9	5.0	6.2	7.8	9.76
Min. skewness [°]	10.4	10.4	10.4	10.4	10.4
Max. exp. ratio [-]	2.8	2.9	2.6	2.3	2.0

At the end, it is found that a mesh of 5 million points provides an excellent trade-off between accuracy and computation time (cf. fig. 8).

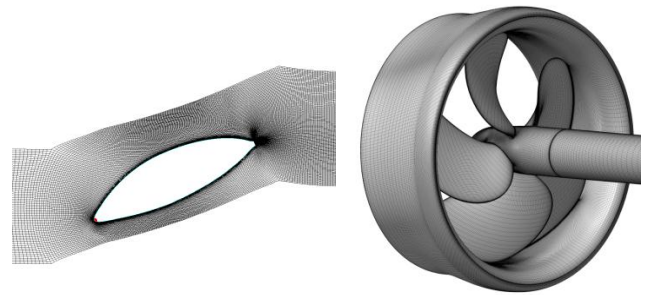


Figure 7: Overview of the final mesh, on the left, a blade to blade view at  $0.2R$ , and on the right, the mesh repetition.

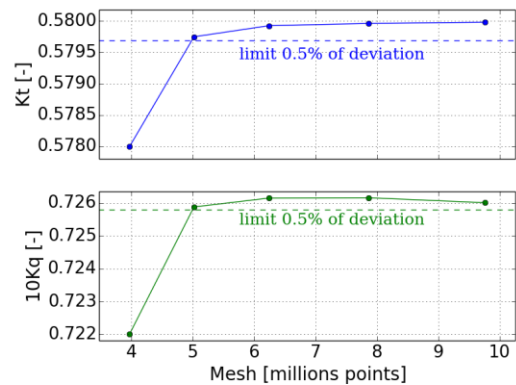


Figure 8: Grid convergence curve for the design operating condition.

##### 5.1.2 Physics and boundary conditions

FINE™/Turbo, used as flow solver, has been validated for open water computations, and shows excellent agreement with regards to experiments, and also to capture cavitation pattern (Salvatore 2009).

FINE™/Turbo is a three-dimensional density-based structured multi-block Navier-Stokes solver using finite volume. Central-space discretization is employed along with multi-grid, local time-stepping and implicit residual smoothing, in order to speed-up the convergence.



For the current propeller, the grid density allows to get a 4 levels grid and a V-cycle for the multi-grid method. In case of low mach number incompressible fluid, time-marching density-based solver lacks of efficiency, a low speed preconditioning is often required to improve the convergence rate. The preconditioning method presented by Merkle et al (1985) is applied.

Standard boundary conditions for a typical open water computation are applied and defined below:

- A static velocity profile and a static turbulence conditions are specified at the inlet;
- An atmospheric pressure is applied at the outlet;
- A slip wall is set on the side wall of the cylindrical domain, which allows to monitor the internal mass flow for convergence behaviour;
- Periodic conditions are used to simulate only one blade passage;
- And the characteristics of the fluid are described in the table 5 below.

**Table 5: Main characteristics of the fluid.**

Fluid model	Incompressible
$\rho$ [kg/m <sup>3</sup> ]	998
$\nu$ [m <sup>2</sup> /s]	1.0453e-06

The choice of the input velocity distribution is dictated by the simulation of the ship at 10km/h and 11.5km/h. It eventually gives the velocity profile at the propeller location (cf. fig.2).

In order to take into account the highly non-uniform wake while assuming a steady state periodic computation, the wake is averaged in the circumferential direction over different radius locations.

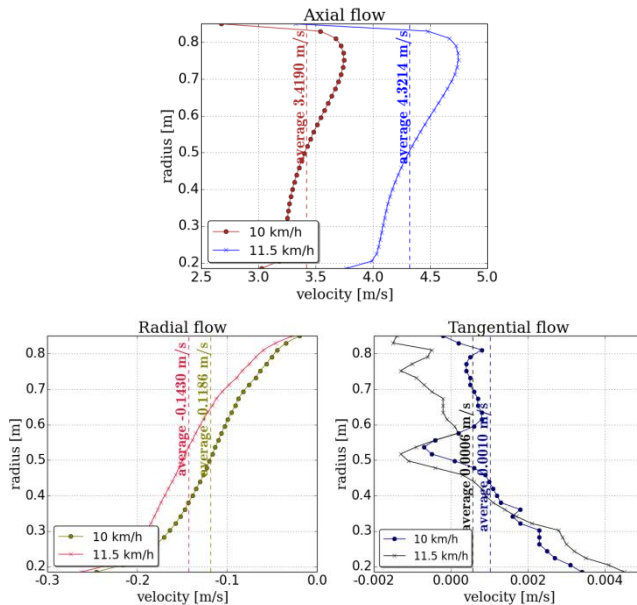


**Figure 9: Circumferential averaging of the wake flow field.**

It can be seen on fig.9, the radial component can be neglected, and the tangential one remains small. Hence only an axial profile is used at the inlet.

The position of the boundary is also important, and requires considerations.

The inlet position should be selected in order to ensure an interaction between the velocity profile and the blade, without creating an upstream extrapolated lower pressure level.

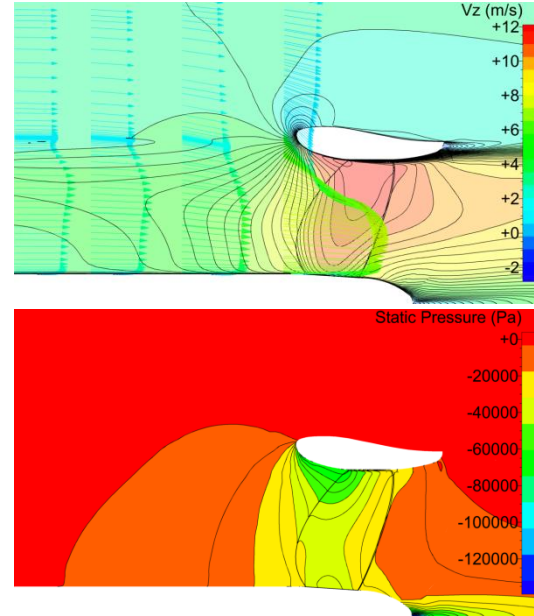


**Figure 10: Meridional view of the simulation using the 11.5km/h velocity profile, with the axial velocity at the top, and the extrapolated pressure at the bottom.**

The distance is manually adapted and set to 1 diameter length, and 5 diameter length for the outlet.

This configuration is used for both operating conditions (10km/h and 11.5km/h).

To simulate the three dimensional environment, Spalart–Allmaras model of turbulence is selected. At the end, a single computation, for 1 operating condition, lasts 26 min on 48 cores.

### 5.1.3 Cavitation inception

Cavitation can have a significant influence over the open water characteristics of the propeller, and thus should be considered when designing and optimizing any marine propeller. The complexity of the physics is real, and designers often use costly cavitation model, to evaluate its presence and the impact of this two phase phenomenon.

In the frame of the optimization, the usage of cavitation model is source of higher CPU cost and can be contradictory with the expected short design process. Hence a meaningful way to predict the cavitation is to compare the pressure level on the blade with the vapour pressure.

In our study, a 15°C fresh water is assumed with a vapor pressure equal to 1700 Pa.

In order to monitor the cavitation, the cavitating volume, or cavity, must be extracted. As the propeller tip position is quite close to free surface position at the design condition, the column of water is neglected. Hence the cavity is computing by mean of an iso-surface of static pressure below the vapour pressure.

This method has proved to give a first idea of the cavitation pattern (Salvatore et al 2009), but must be validated by a more accurate model afterwards.

But in the case of the optimization, it is an excellent quantity to monitor.

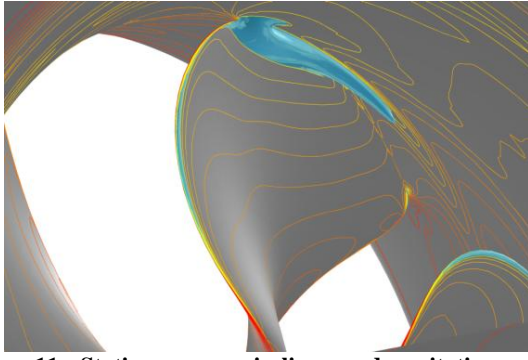


**Figure 11: Static pressure isolines and cavitating cavity, represented by an iso-surface in blue, for the design condition (10 km/h).**

The cavity of about 400 ml remains small compared with the overall size of the propeller. Besides, Carlton (2012) indicates that a moderate level of cavitation may not affect the propeller hydrodynamics performances, so the constraint on the cavitation volume should not be too strict during the optimization.

## 5.2 Selection of the uncertain parameters

### 5.2.1 Geometrical uncertainties

Manufacturing tolerances, for marine propellers, are ruled by *ISO* norms such as the *ISO-484-2* (2015) for any marine propeller between 0.80 and 2.50m .

The tolerances are usually expressed as a lower and an upper deviation from a nominal value. Those extrema are taken to represent a statistical tolerance by means of a probability density function (cf. fig.12).

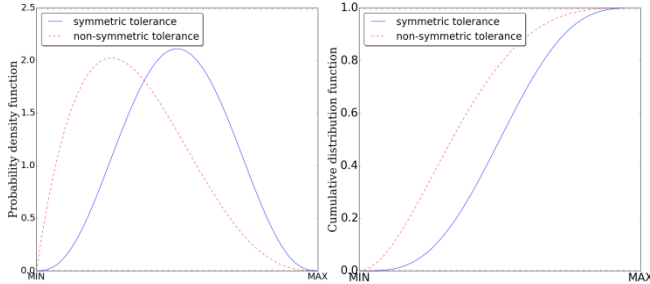


**Figure 12: PDF and CDF for symmetric and non-symmetric distributions.**

In this paper a beta-distribution is used and determined from the *ISO* extrema which is a percentage of the deviation compared to the nominal design value.

**Table 6: Definition of each tolerance in case of a S-class manufacturing accuracy.**

	Plus tolerance	Minus tolerance
Radius	0.2% (not less than 1.5mm)	0.2% (not less than 1.5mm)
Rake	0.5%	0.5%
Blade thickness	2% (not less than 2mm)	1% (not less than 1mm)
Blade chord	1.5% (not less than 7mm)	1.5% (not less than 7mm)

Those extrema are globally prescribed by four accuracy classes, ranging from the most restrictive to the widest tolerances. In this test case, the S-class tolerance is used, which represents the most accurate and restrictive one.

The tolerances definition is of importance, because the final parametric modeller of the propeller has to be defined taking into account the means of tolerance measurements.

### 5.2.2 Operational uncertainty

Inland vessels operate seldom at the same working regime. The ship may be navigating at different speeds, especially speeds higher than the design point, or with different loadings inducing different draughts (cf. fig.1).

Those variations might change the ship wake, influencing the operating regime of the propeller.

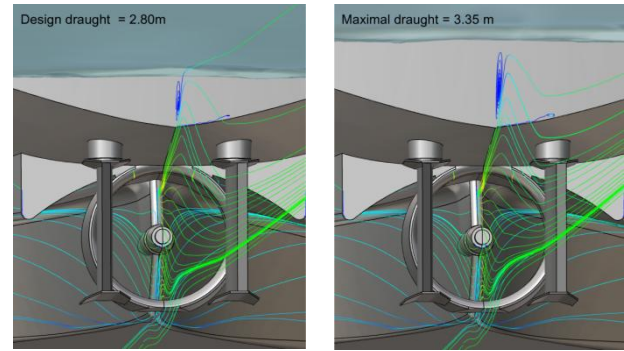


**Figure 13: Streamlines, colored by the velocity magnitude, at the wake of the ship for different draughts.**

In this manner, two resistance computations are performed with two different draughts, nominal and maximal draughts (cf. tab. 1). The nominal wake is then computed.

Fig.14 shows the difference in the velocity field at the propeller location. In order to enlighten the variation of the axial velocity, a radial averaging is performed, and shows a maximal variation of 3%. Hence, a symmetric *PDF* is defined using as extrema the maximal variation.

The wake axial profiles (cf. fig.9) are going to be shifted by this variation during the *UQ* computations.

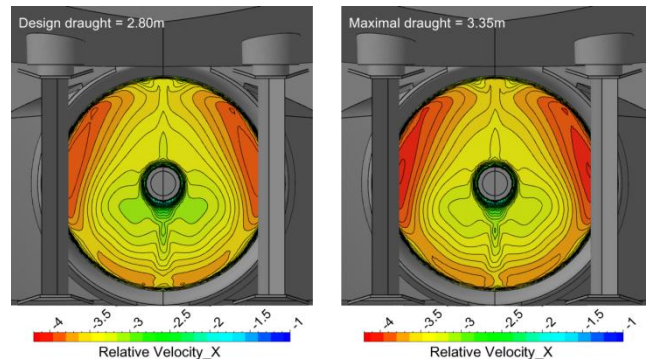


**Figure 14: Relative axial velocity at the propeller location for the design speed condition under two different draughts.**

## 5.3 Parametric definition of the propeller

In order to construct the parametric model, the target is first sliced at different radius locations (cf. fig. 15). From those sections, a parametric topology is used to define the section profile and camber.

The stacking of each section, in other words, their relative positions, defines the rake in the meridional direction and the skewness in the tangential one. Both meridional and tangential laws are parametrized using a Bezier of 6 control points.

The profile is defined using a B-spline curve of 6 control points and the camber using a Bezier of 3 control points. This Bezier curve also defines the local profile pitch and chord.

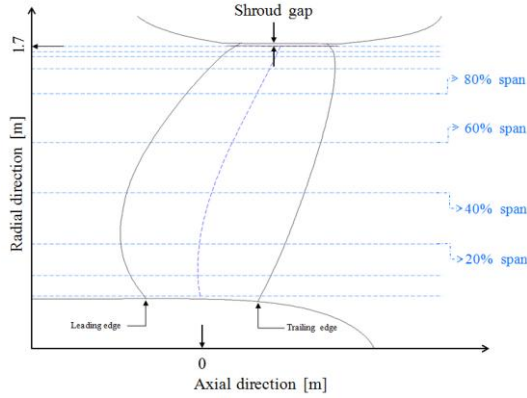


**Figure 15: Location of the slicing sections along the span.**

The choice of the sections locations is determined by the *ISO*. Indeed, the *ISO* requests manufacturers to verify the deviation at different locations on the blade, i.e. 20%, 40%, 60% and 80% of the radius. Thus, it is better to control the uncertainty parameter and apply a correct evaluation of its impact when both manufacturing measurement and parametric modification are performed at the same radius.

As suggested by Nigro et al (2018), the parametrization induces modifications and deviations from the initial target geometry. In case of uncertainty study, it is crucial to represent the initial target geometry with a high accuracy, such that the previously discussed deviations are significantly lower than the geometrical uncertainty. This verification is performed on two levels:

- First the parametric and the target geometry are visually compared;
- Then the *CFD* simulations are juxtaposed.

### 5.3.1 Accuracy of the geometry parameterization

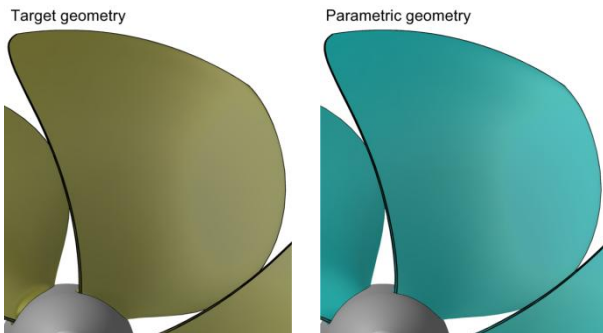


**Figure 16: Comparison between the target (left) and the parametric geometry (right).**

During the parametrization, a global visual inspection is performed, in order to detect strong deviations and therefore adapt the parametric topology to fit accurately the initial target geometry.

The result of this process is demonstrated by *figure 16*. It can be seen that both geometries do not display significant differences. The parametric model respects globally the shape of the initial target one, so a close-up is performed on different sections of the blade.

It eventually shows discrete geometrical deviations and amount locally up to 500 microns (cf. *fig.17*), where the uncertainty is equal to 2 mm for the thickness and 7 mm for the chord.

In conclusion, the local modifications are in the overall lower than the manufacturing tolerances.

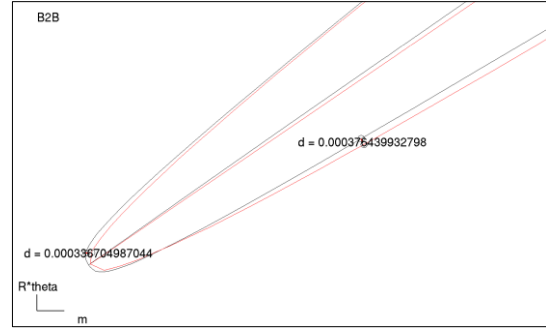


**Figure 17: Close-up at the leading edge part at 60% of the span.**

### 5.3.2 Influence of the parametric model on the deterministic results

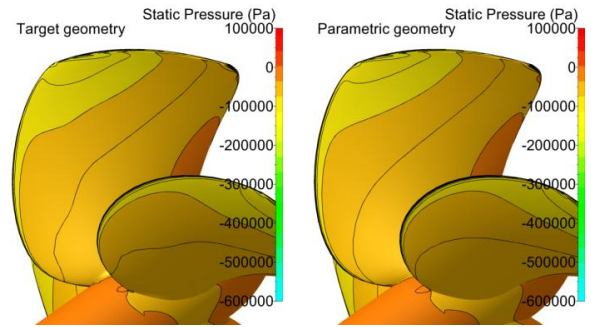


**Figure 18: Comparison of the pressure field between the target (left) and the parametric geometry (right).**

The influence of the error introduced by the parametric model on the *CFD* results must be assessed.

This also allows validating the parametric model as starting design for the optimization.

Eventually, the flow field does not show any serious difference (cf. *fig. 18*), and the overall results are within 1%. It validates the parametric model and also implicitly confirms that even a small variation in the geometry discretely affects the performances. It is important to underline that the evaluation of the parametric model accuracy has an importance in the *RDO* framework. For deterministic optimization, this procedure can be more flexible, since the geometry is deformed in any case.

**Table 7: Comparison of the target and parametric geometry.**

	Target	Parametric	$\frac{Parametric - Target}{Target} \times 100$
$T [N]$	1.411e+05	1.402e+05	-0.71%
$Q [Nm]$	2.959e+04	2.985e+04	+0.87%
cavity	400 ml	398 ml	-0.5%



## 6 DETERMINISTIC AND NON-DETERMINISTIC OPTIMIZATION

### 6.1 Deterministic optimization

#### 6.1.1 Overall formulation

The design parameters consist in a total of 18 variables:

- 4 for the sections profile law;
- 2 for the chord law;
- 3 for the local pitch law;
- 3 for the camber law;
- 6 parameters for the skewness and the rake laws.

The thickness is kept constant, as the modification would induce a change on the structural computation of the bending moment. As suggested in section 3.2, the *DoE* is sampled by 90 designs. For each design in the *DoE*, the overall quantities (1) and (2) are automatically post-processed, along with the cavitation volume and the open water efficiency (6):

$$\eta = \frac{K_t}{K_q} \frac{J}{2\pi} \quad (6)$$

Two operating conditions are considered and linked to the ship speeds (cf. *table 1*), 10 km/h and 11.5 km/h. The revolution rate of the propeller is kept constant. Thus, only the inlet flow condition is changed (cf. *fig.9*).

The overall objectives and constraints are the following:

- Improving the overall open water efficiency  $\eta$  by using an aggregated formulation of both operating conditions  $0.7 \times \text{design speed} + 0.3 \times \text{off design speed}$ ;
- Maintaining the axial thrust as it is a requirement for the contractual ship design speed. So,  $K_t$  is constrained and equal to 0.58;
- Not deteriorating the performance, by keeping similar cavitation behaviour. As this constraint should be flexible (cf. *section 5.1.3*), it is decided to keep the volume below 800 ml;
- Simulation should be converged. The criteria, to decide whether the simulation is converged or not, is based on the difference between the inlet and outlet mass flow. This deviation should not exceed 0.1%, otherwise the sample is rejected.

#### 6.1.2 Optimization outcome

The deterministic mono-objective optimization reaches an optimum meeting all constraints within 30 iterations. The final optimum shows an increase in the weighted efficiency of about 2.26% relatively (i.e. almost 1% in absolute), while the thrust is maintained and the cavitation is below the fixed threshold.

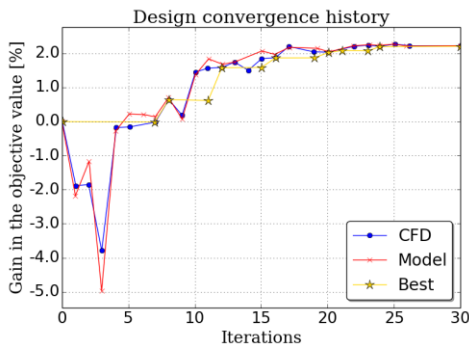


Figure 19: Convergence history of the mono-objective deterministic optimization, model represents the surrogate model results.

The *table 8* summarizes the performances of the deterministic optimum compared to the baseline, the initial parametric geometry, and *figure 24* shows the geometrical differences.

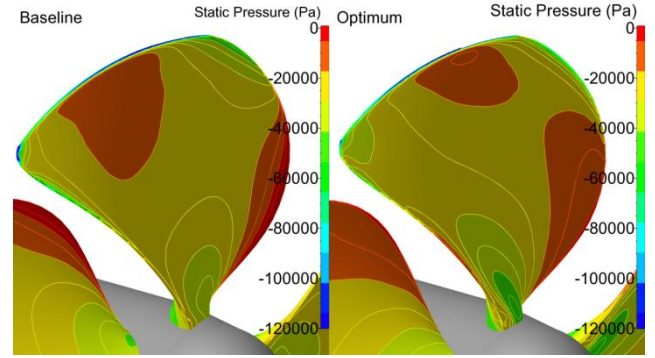


Figure 20: Static pressure comparison between the baseline (left) and the deterministic optimum (right).

When looking at the downstream velocity field, it can be seen that the tangential component of the optimum is less pronounced than the baseline (cf. *fig 21*). This indicates a more aligned flow and consequently a higher efficiency.

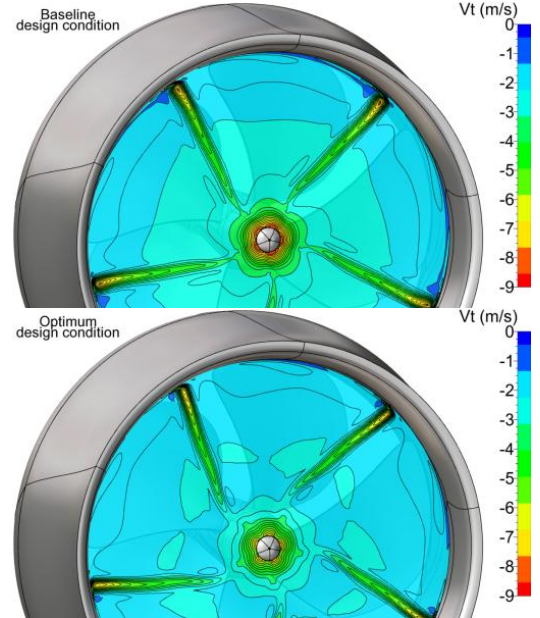


Figure 21: Tangential velocity behind the trailing edge for the baseline (upper picture) and the deterministic optimum (lower picture).

This is also implied by the *figure 22*, where the midspan profile drag of the baseline is higher.

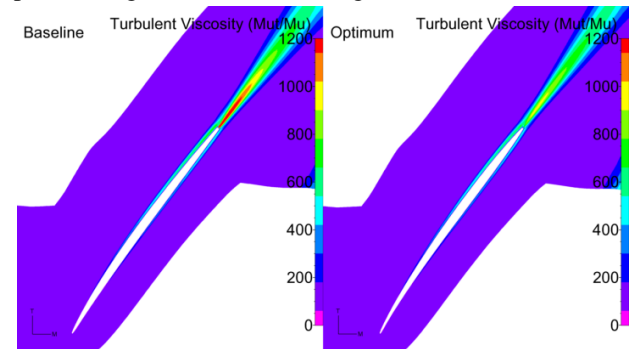
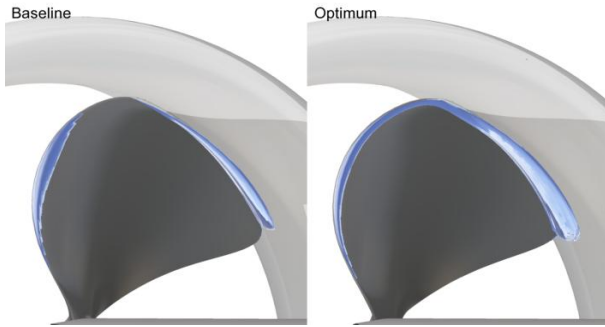


Figure 22: Midspan blade to blade view of the turbulent viscosity ratio between the baseline (left) and the deterministic optimum (right), at the design condition.



For the cavitation modelling, it can be seen that the improvement in the propeller performances is highly constrained by the cavitation volume (cf. *table 8*), as the final optimum features a cavity closed to the constraint value *800 ml*. In other words, the optimizer cannot find a better optimum without exceeding this constraint.



**Figure 23: Cavitation simulation for the baseline (left) and the optimum (right).**

Two steady cavitation simulations are eventually run to validate the actual performances of the propeller (cf. *fig.23*), and demonstrate that both designs suffer minor losses in their respective performances, validating the optimization procedure.

However, both designs feature bubbles-like cavitation at the tip. This is problematic in terms of vibration and comfort. As it is suggested in *figure 11*, the cavity is attached to the nozzle shape, which indicates that the interaction between the propeller blade and the duct influences strongly the cavity size. Thus the nozzle shape should be also optimized, which is not the case in this paper.

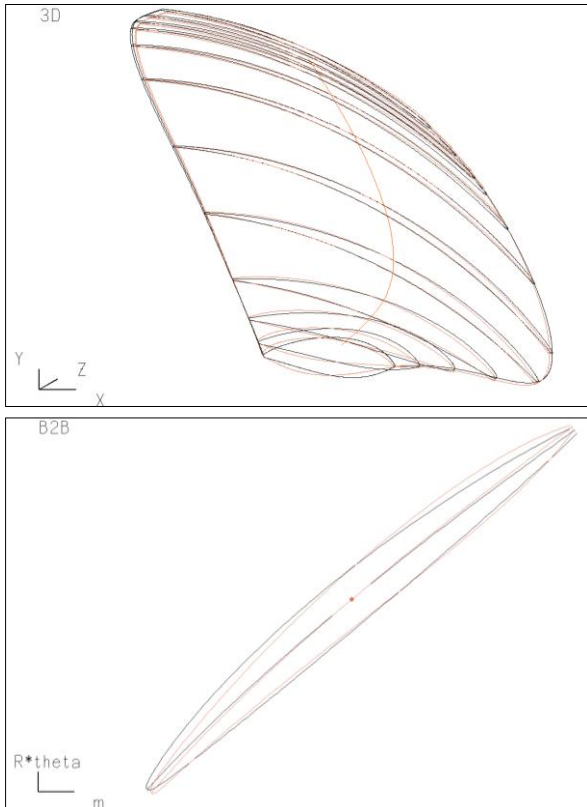


**Figure 24: Overlapping of the optimum (in red) and the baseline (in black) for the 3D and the blade to blade (at  $0.2R$ ) views.**

**Table 8: Comparison of the baseline and the optimum performances.**

		Baseline	Optimum
Design condition 10km/h	$K_t$	0.58	0.58
	$K_q$	0.072	0.0705
	$\eta$	0.39	0.401
Off-design condition 11 km/h	$K_t$	0.506	0.505
	$K_q$	0.068	0.0667
	$\eta$	0.419	0.428
Weighted $\eta$		0.399	0.408
Cavity [ml]		398	769

## 6.2 Non-deterministic optimization

### 6.2.1 UQ simulations

An initial *UQ* study is performed with 13 uncertainties:

- 4 uncertainties for 4 different sections chord defined with a symmetric beta *PDF*;
- 4 uncertainties for 4 different profiles thickness defined with a non-symmetric beta *PDF*;
- 1 uncertainty for the rake, which represents the linear position of the tip compared to the root of the blade, defined with a symmetric beta *PDF*;
- 1 uncertainty for the gap between the blade and the duct, defined with a symmetric beta *PDF*;
- 1 uncertainty for the axial velocity defined in section 5.2.2.

By using a sparse grid level 1, 32 deterministic computations need to be run. Indeed, Nigro et al (2017) proved that a level 1 already provides accurate results on the mean and the variance, which is sufficient for the *RDO*.

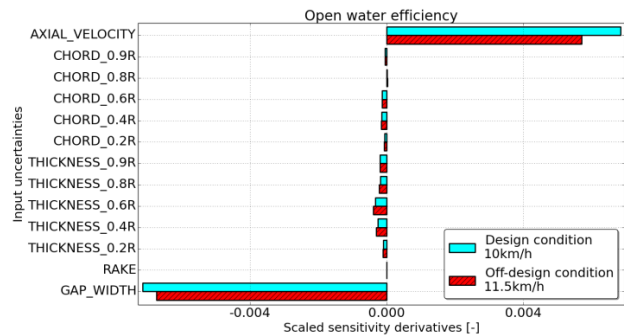


**Figure 25: Scaled sensitivity derivatives of the open water efficiency for both operating points, with 13 uncertainties.**

Scaled sensitivity derivatives (section 4.1.3) are then computed, and show that the main influencing components are the axial velocity and the gap between the duct and the tip. This analysis is quite logical, because the efficiency  $\eta$  is function of the advance ratio of the propeller  $J$ , also function of the blade diameter and the axial velocity (6).

Moreover, the uncertainties for the thickness having the lowest standard deviation are clearly more important than

those for the chord. This is also logical considering the fact the thrust and torque are directly influenced by each blade profile thickness.

From that analysis, it is decided to merge all chord and thickness uncertainties together. The change in the shape of the blade profile is controlled by a single section. And the rake uncertainty is neglected. This reduces the number of uncertainties to 4, and the number of deterministic computations is now 10, for a single operating condition.

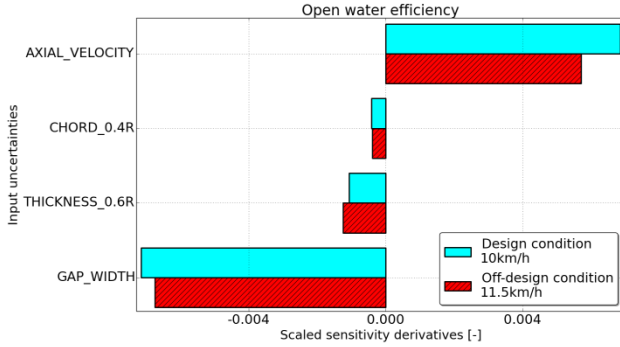


**Figure 26: Scaled sensitivity derivatives of the open water efficiency for both operating points with 4 uncertainties.**

The scaled sensitivity derivatives show a similar trend between 13 and 4 uncertainties (cf. fig. 25 & 26).

Moreover, a normal distribution is reconstructed in order to display the difference in the mean and the variance (cf. fig.27).

It can be concluded that the reduction of the number of uncertainties did not impact the statistical moments results. Hence, 4 uncertainties are used during the *RDO*.

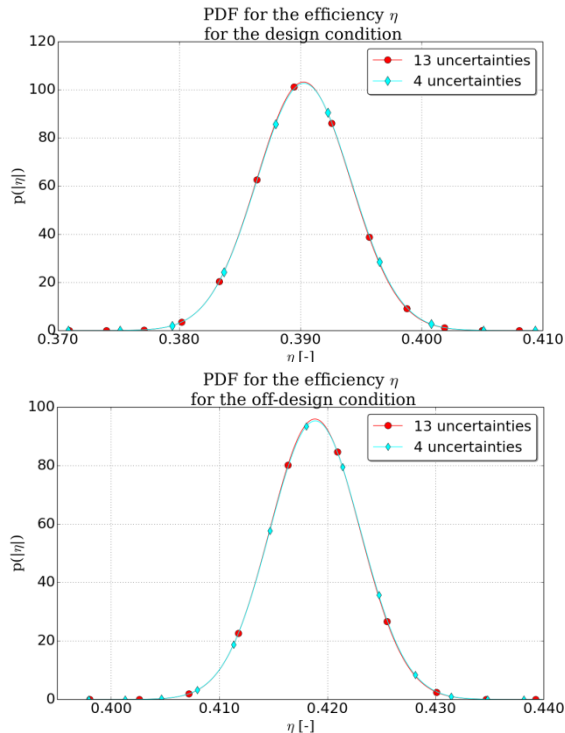


**Figure 27: Normal distribution using the mean and standard deviation for both operating conditions and 13 and 4 uncertainties.**

The scaled sensitivity analysis can also be useful for analysing the uncertainties influence over other key quantities, such as the cavitation volume, helping to identify critical variabilities.

Indeed on fig.28, it can be seen that all geometrical and operating conditions strongly impact the cavity size, and might increase its volume by 4% when decreasing the axial velocity and 3.5% when increasing the propeller duct gap distance.

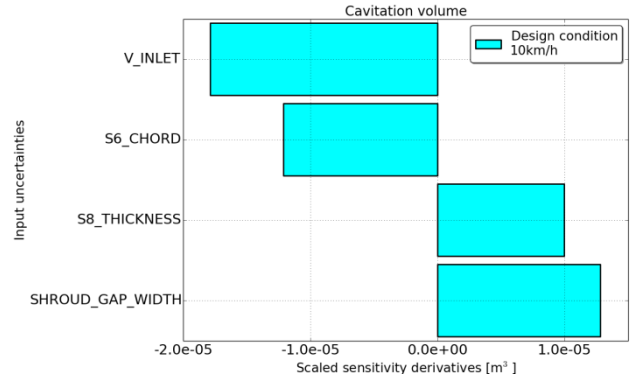


**Figure 28: Scaled sensitivity derivatives of the cavity volume for the design condition.**

### 6.2.2 Robust optimization outcome and comparison with the deterministic optimum

The same design parameters are used, with 4 additional uncertainties for the *DoE* generation (cf. section 6.2.1).

The same operating points are considered.

However the formulation of the *RDO* is as followed:

- Improving the overall open water efficiency  $\eta$  by maximizing its mean value  $\mu(\eta)$ , using the same aggregated formulation for both operating conditions;
- And also improving the robustness of the design by minimizing the standard deviation of the same efficiency  $\sigma(\eta)$ ;
- Maintaining the mean axial thrust,  $\mu(K_t)$  is constrained and equal to 0.58;
- Not deteriorating the performance, by keeping  $\mu(cavity)$  below 800 ml.

In consequence, it can be seen that the *RDO* formulation is multi-objectives and the outcome is the Pareto front. The same number of iterations is used. For each iteration, 10 deterministic *CFD* computations, per operating condition, are performed in order to compute the statistical moments.

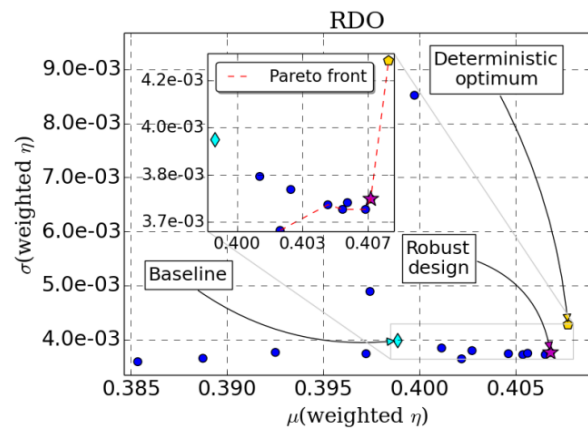


**Figure 29: RDO history and Pareto front outcome.**

Figure 29 clearly displays a robust design among the non-dominated samples, which manages to reduce the standard deviation by 6 % and the mean efficiency is increased by 2%.

It is decided to select a single robust design, because it features the best trade-off in terms of statistical moments enhancement.

Moreover, a *UQ* study is performed on the deterministic optimum and also shows an increase of the mean efficiency, but also an increase of the standard deviation of about 7.4% (cf. *fig.30*). Hence, the deterministic optimum is consequently less robust, but is still located on the Pareto front.

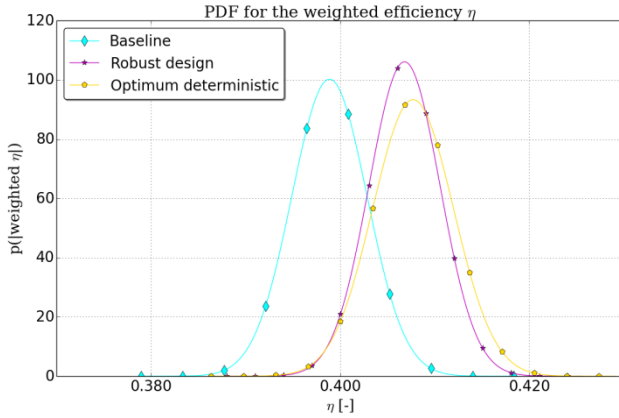


**Figure 30: Normal distribution of the baseline, the robust and deterministic optima.**

Moreover, the scaled sensitivity derivatives (cf. *fig.31*) reveal that the influence of the axial velocity and the diameter are still the largest.

However, the geometrical uncertainties show a discrete reduction in their respective influences for the robust design. This explains the decrease of the standard deviation.

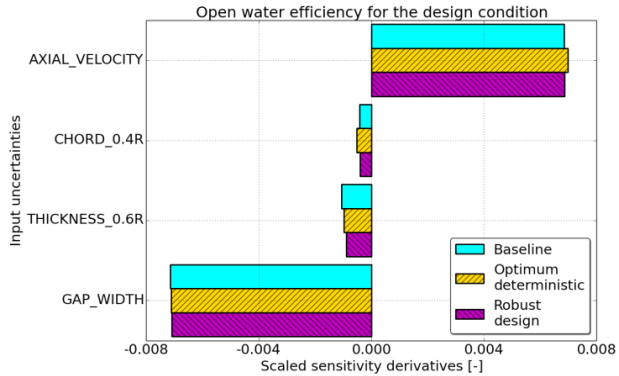


**Figure 31: Scaled sensitivity derivatives at the design condition for the baseline, and the robust and deterministic optima.**

*Figure 32* shows a comparison of the propeller blade shapes, the deterministic and the robust. The robust design features a higher skewness in contrast to the deterministic optimum and the baseline (cf. *fig.24*). The explanation of the geometrical differences comes from the robust optimization formulation.

Indeed, the deterministic optimization aims at localizing the best design for a single objective formulation, whereas the *RDO* proposes a set of non-dominated designs with the objective to improve both performances and robustness.

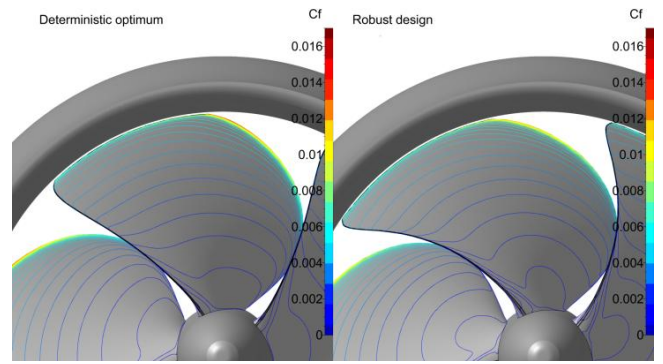


**Figure 32: Comparison between the deterministic optimum (left) and the robust design (right).**

### 6.2.3 Computational cost of the robust design optimization compared to the deterministic optimization

In both cases, 5 samples per dimensions are used in the initial *DoE*. The non-deterministic *DoE* have 4 extra uncertainties, leading to an increase of 20 additional designs in the *DoE*.

For the optimization, the same amount of iterations is used. However each robust iteration performs *UQ* simulations. At the end the robust optimization leads to a computational overhead of 3.42.

**Table 9: Detail of the computational cost comparing a robust design optimization and the deterministic optimization. The computation of the CPU Hours assumes that 1 CFD has a cost of 20.784 CPU hours (26 min on 48 cores).**

	Deterministic optimization	Robust design optimization
Number of samples in the <i>DoE</i>	90	110
Total number of CFD runs for the <i>DoE</i>	180	220
Number of CFD per optimization iterations	2	20
Number of optimization iterations	30	30
Total number of CFD runs for the optimization	60	600
Total number of CFD runs	240	820
Computational cost [CPU Hours]	4988.16	17042.88

## 7 CONCLUSION

In this paper, two design optimization studies were performed: a deterministic optimization and a robust optimization accounting for uncertainties. Since the investigated ducted propeller was subject to several operating conditions, two were considered: the design condition, which was used to draw the initial baseline geometry, and an arbitrary off-design condition based on the maximal cruising speed of the vessel.

As the cavitation was also of importance, a low *CPU* cost modelling based on the pressure field was used and provided interesting information.

Indeed the first deterministic optimization indicated the relevance of considering cavitation modelling. Indeed, the optimization outcome demonstrated the trade-off between performances improvements and cavitation criteria.



Strictly speaking, the optimizer was restrained in the search of a better design due to the constraint in the cavitation volume. However, the performances can be further improved by including the nozzle shape parameters in future optimizations.

The second optimization was the robust design optimization that aimed at improving the performances while reducing the vulnerability of the design performances with respect to both operational and geometrical variabilities. The evaluation of those variabilities was performed by uncertainty quantification simulations. It was also observed that the *UQ* simulations can also play a major role in the design process for identifying critical manufacturing variabilities over key quantities of interest, such as cavitation or efficiency.

Eventually, both deterministic and robust optimum were compared, and as expected the robust design increased the performances and the robustness.

Moreover, the deterministic optimum was also located on the Pareto front, which might indicate that the inputted manufacturing variabilities were small enough to guarantee an acceptable stable behaviour, which was the expected results when using the most precise and costly S-class tolerance. Knowing the real-life performances can be assessed, the propeller designers can now try to apply coarser and less expensive manufacturing tolerance, and use the proposed approach to optimize the design accounting for several variabilities and operating conditions.

## 8 REFERENCES

- Bundesanstalt für wasserbau (2016). 'Driving Dynamics of Inland Vessels', BAW.
- Carlton, J.S. (2012). 'Marine Propellers and Propulsion', Butterworth-Heinemann.
- Coley, David A. (1999). 'An Introduction to Genetic Algorithms for Scientists and Engineers', World Scientific.
- Golub, G.H. & Welsch, J.H. (1969). 'Calculation of Gaussian Quadrature rules', Math. Comp. 23:221-230.
- Insights, global market (Apr. 2018). 'Inland Waterways Vessels Market to Hit \$2.25 Billion by 2024.' Global Trade Magazine, The Authority For US Companies Doing Business Globally.
- ISO 484-2 (2015). 'Shipbuilding -- Ship screw propellers -- Manufacturing tolerances -- Part 2: Propellers of diameter between 0,80 and 2,50 m inclusive'.
- Loeven, G.J.A., Witteveen, J.A.S., and Bijl, H. (2017). "Probabilistic Collocation: An Efficient Non-Intrusive Approach for Arbitrarily Distributed Parametric Uncertainties", 45th AIAA Aerospace Sciences Meeting and Exhibit, Aerospace Sciences Meetings.
- Merkle et al. (1985). 'Application of Time-Iterative Schemes to Incompressible Flow', AIAA Journal, Vol. 23, No 10, pp. 1518-1524.
- Nigro, R., Wunsch, D., Coussement, G., and Hirsch, C. (2017). 'Uncertainty Quantification in Internal Flows', 55th AIAA Aerospace Sciences Meeting.
- Nigro, R., Wunsch, D., Coussement, G., and Hirsch, C. (2018). 'Robust design in turbomachinery application', Findings and Best Practice Collected During UMRIDA, a Collaborative Research Project (2013–2016) Funded by the European Union pp. 495-511.
- Salvatore et al (2019). 'Propeller Cavitation Modelling by CFD - Results from the VIRTUE 2008 Rome Workshop', SMP'09.
- Sihn et al (2015). 'A Green and Economic Future of Inland Waterway Shipping.', Procedia CIRP vol 19 pp. 317–322.
- Smolyak, S. (1963). 'Quadrature and Interpolation Formulas for Tensor Products of Certain Classes of Functions', Doklady Akademii Nauk SSSR Volume 4, pages 240-243.
- Turgeon et al. (2011). 'Parametric uncertainty analysis for thermal fluid calculations', Nonlinear analysis 47 4533–4543.